

## Effect of Mg Content on Stress Corrosion Cracking of Al-X Mg Alloys

G. X. Liu<sup>1,2</sup>, M. Wu<sup>1\*</sup>, Y. J. Yang<sup>1</sup>, X. Y. Liu<sup>4</sup>, C. C. Wang<sup>3</sup>, J. C. HUANG<sup>5</sup>, X. Wang<sup>4,\*</sup>

<sup>1</sup> College of Petroleum Engineering, Liaoning Shihua University, Fushun 113001, P. R. China.

<sup>2</sup> College of Pipeline and Civil Engineering, China University of Petroleum, Qingdao, 266555, China.

<sup>3</sup> State key laboratory of rolling and automation, School of Materials Science and Engineering, Northeastern University, Shenyang 110819, P. R. China.

<sup>4</sup> School of Mechanical Engineering, Liaoning Shihua University. Fushun 113001, P. R. China

<sup>5</sup> Institute for Advanced Study, Department of Materials Science and Engineering, City University of Hong Kong, Kowloon, Hong Kong.

\*E-mail: [lgx1101@gmail.com](mailto:lgx1101@gmail.com), [wangxu@lnpu.edu.cn](mailto:wangxu@lnpu.edu.cn)

Received: 5 November 2018 / Accepted: 29 December 2018 / Published: 7 February 2019

---

The stress corrosion cracking (SCC) behavior of Al-Mg alloys with different Mg contents (Al-X Mg, X=2.5, 4.5, 6.3) were researched by transmission electron microscopy (TEM), electrochemical tests and constant extension rate tensile experiments combined with scanning electron microscopy (SEM). The corrosive environment for the SCC tests was 3.5 wt.% NaCl solution. Electrochemical results indicated that corrosion potential decreased with an increase in Mg content, while corrosion current density ( $i_{\text{corr}}$ ) increased significantly. The Al-2.5Mg alloy exhibited the lowest  $i_{\text{corr}}$  among the three investigated compositions, indicating that the Al-2.5Mg alloy exhibited the best corrosion resistance, which was corresponding to the EIS results. TEM observation results showed that the number of precipitates rises with an increase in Mg content. In the SCC tests, collinear bilateral pulls along double-sided specimens have been applied in constant extension rate tensile experiments. The Al-2.5Mg alloy exhibited the lowest susceptibility to SCC; the slopes of the da/dt-K curves during stage II increase with an increase in Mg content in the Al-Mg alloys and da/dt of Al-6.3Mg is the fastest at a given stress intensity factor, implying that stress corrosion is more and more serious with the increase of Mg content in the Al-Mg alloys. SEM micrographs has shown that the fracture is chiefly intergranular and transgranular and the stress corrosion crack surface is mainly intergranular corrosion (IGC).

---

**Keywords:** Al-Mg alloys; Mg Content; Corrosion susceptibility; Stress corrosion cracking;

## 1. INTRODUCTION

With the increasing use of marine resources, Al alloys are being more and more popular among structural materials for lightweight ships [1]. Marine-grade 5xxx Al alloys are widely employed as anti-rust Al alloys because of their combination of good corrosion resistance, weldability, and formability and moderate strength characteristics [2-5]. These enhanced characteristics are developed in part by the Mg content of the alloy, which is typically greater than 3 wt.%. Although Al-Mg alloys are designed to meet certain strength requirements for use in body structures [6], Al-Mg alloys become vulnerable to stress corrosion cracking (SCC) and intergranular corrosion (IGC) when the Mg content reaches 3.5 wt.%. From a corrosion perspective, the presence of the  $Mg_2Al_3$  phase ( $\beta$ -phase), in particular, causes major sensitivity to IGC and SCC, especially in solutions that contain  $Cl^-$  ions [7-9].

The  $\beta$ -phase is anodic relative to the Al matrix and will be selectively dissolved in seawater, thus, the continuous distribution of the  $\beta$ -phase along the grain boundaries is closely related to sensitivity to IGC, which has been investigated in previous reports [10-12]. When Al-Mg alloys are upon exposure to corrosive electrolyte such as seawater, the potential difference between the  $\beta$ -phase precipitate and the Al matrix causes formation of a microgalvanic cell. Therefore, the  $\beta$ -phase precipitates along the grain boundaries dissolve gradually, making grain boundaries more susceptible to IGC [13-15]. The common SCC mechanism in Al-Mg alloys is accelerated by IGC and is localized by applied stress, moreover, the chemicals permeating the structure also play a role. Buczynski and Kelly [16] researched the corrosion behaviour of  $Mg_2Al_3$  and AA5083 in various electrolytes and found that, upon exposure to acidic conditions,  $Mg_2Al_3$  dissolved faster than the Al matrix. Song [17] used Auger electron spectroscopy to investigate the 7050 Al alloy exposed to humid air, found that the crack velocity was positively related to Mg segregation at grain boundaries. Liu [18, 19] researched Mg corrosion in bulk  $Mg_2Al_3$  tested in an  $Na_2SO_4$  solution as observed by X-ray photoelectron spectroscopy and secondary-ion mass spectrometry. As an added factor of concern, the mechanism of  $\beta$ -phase-related corrosion in Al-Mg alloys should be evaluated to determine the SCC susceptibility of these components [20]. Two fundamental issues concerning the SCC of Al-Mg alloys need to be investigated: (1) effect of Mg content on stress corrosion cracking and (2) the contributions of the  $\beta$ -phase precipitates and the surrounding grain-boundary area to crack advancement.

Although earlier reports have shown that the existence of stable Al passivation film is hardly affected by Mg segregation, and the stability of the film will not be altered when the Mg content is less than 3 wt.% [21, 22], H permeation data in earlier reports and the large H reduction observed with corrosion of the  $\beta$ -phase can support the mechanism of H-induced crack growth [23]. However, the test data of H permeation remain unconfirmed because related experiments have not been repeated and covered in the open literature. Hence, the purpose of this study was to quantify the role of Mg along the grain boundary in SCC and to explain the relationship between the volume fraction of  $\beta$ -phase along grain boundary and the crack propagation velocity in Al-Mg alloys [24].

Most of the previous researches on Al-Mg alloys mainly focused on the effects of Mg contents on mechanical properties and corrosion resistance; however, the effect of Mg content on SCC of Al-Mg alloy has not yet been reported after different immersion time. Potentiodynamic polarization curves, electrochemical impedance spectroscopy (EIS) measurements, and SCC experiments were

adopted to research performance of samples with different Mg contents (Al-2.5Mg, Al-4.5Mg, and Al-6.3Mg) in 3.5 wt.% NaCl solution.

## 2. EXPERIMENTAL PROCEDURE

### 2.1 Microscopy Analysis of Grain-boundary Segregation and $\beta$ -Phase Precipitation

The specimens used for the tests were prepared from Al alloy hot-rolled plate; the chemical components of the specimens are shown in Table 1. The  $\beta$ -phase was observed by optical microscopy (Leica DMI5000M) and transmission electron microscopy (TEM; JOEL JEM-2100F). Optical metallography observation was performed on polished samples after the samples were etched with 0.5 wt.% hydrofluoric acid for 40 s. The fracture surface morphology was observed by means of scanning electron microscopy (SEM; HITACHI SU8000).

**Table 1.** Chemical Composition of Aluminum Alloys

Alloy	composition (wt.%)						
	Si	Fe	Cu	Mn	Zn	Ti	Al
Al-2.5Mg	0.25	0.08	0.1	0.1	0.1	--	bal
Al-4.5Mg	0.4	0.08	0.1	0.5	0.25	0.15	bal
Al-6.3Mg	0.4	0.08	0.1	0.5	0.2	0.03	bal

### 2.2 Electrochemical Analysis

Experiments of potentiodynamic polarization curve measurements were performed in 3.5 wt.% NaCl solution. All electrochemical experiments were conducted at room temperature after stabilization of the open circuit potential. All tests were conducted under ambient conditions using a three-electrode cell, where a saturated calomel electrode and a Pt electrode were adopted as the reference electrode and the auxiliary electrode, respectively; the exposed surface area of the Al-Mg alloy was 1 cm<sup>2</sup>. The open circuit potential (OCP) was monitored for 60 min before the commencement of EIS measurements and polarization at a scan rate of 0.5 mV/s. A sinusoidal potential perturbation of 10 mv were applied to conduct the tests of EIS measurements. The frequency scope of the impedance spectra was 100 kHz to 10 mHz. All tests were carried out not less than four times to ensure reproducibility.

### 2.3 SCC Experiments

Constant extension rate tests were carried out on dog bone shaped Al-6.3Mg specimens, and the specimens were cut from rolled plates both in the plate-rolling direction and across the rolling direction. The static properties were shown in Figure 1, as can be seen, the specimen across the plate-rolling direction showed lower ultimate strength and elongation, which indicated that SCC sensitivity of Al-6.3Mg specimen along the plate-rolling direction was higher.

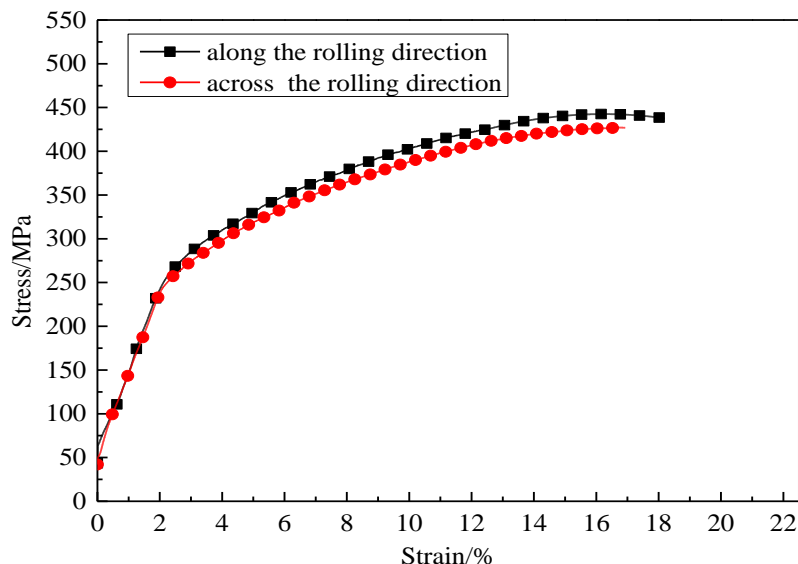


**Figure 1.** Monotonic tensile curves of Al-6.3Mg aluminum alloy

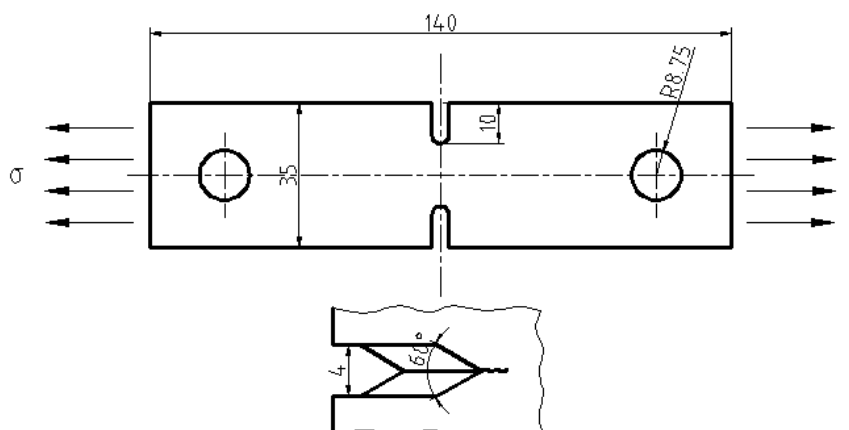


**Figure 2.** Collinear bilatera pulled along double-side specimen used in the SCC experiments

Collinear bilateral pulls along double-sided specimens of Al-Mg alloy were adopted for SCC experiments to evaluate the SCC degree of the Al-Mg alloys. Tensile tests were carried out according to ASTM standard E647 [25]. The specimens were cut from rolled plates across the plate-rolling direction, as can be seen in Figure 2, the rolling direction was across specimen axis [26], the thickness of the specimen is 2 mm. The specimens were sanded using sandpaper of 80 to 2000 grain sizes. The stress were applied along the specimen axis and crack propagation direction was along the plate-rolling direction. Each specimen was notched using a PLD-20 electrohydraulic servo fatigue testing machine in tension-tension loading on both sides of the specimen at the same time to bring about a 4mm in wide, 10 mm in length notch. Notched specimen experiments were carried out in free air through fatigue loading. In order to research the role of Mg content in subsequent SCC performance, tensile loads were applied to the Al-Mg alloy specimens at a constant strain rate ( $10^{-4}$  mm/s). Samples were tested to failure in constant extension rate test, and the fracture morphology was studied using SEM.

### 3. RESULTS AND DISCUSSION

#### 3.1 Microstructure

Figure 3 shows the microstructure of the investigated Al-Mg alloy. The dark granular precipitates observed in the Figure are  $\beta$ -phase; Figure 4 shows the characteristics of the distribution of grain-boundary precipitates (GBPs) for all three alloys, as observed by TEM. As exhibited in Figure 4, the number of precipitates rises with an increase in Mg content. The  $\beta$ -phase precipitates are usually nanocrystals and tend to form rod-like particles; therefore, they are very unusual in structure and morphology. The small granular  $\beta$ -phase is discretely distributed along grain boundaries and throughout the grains in Al-Mg alloys. Figure 4(c) shows that the Al-6.3Mg alloy exhibits the highest area fraction of GBPs and the GBPs are distributed continuously at the grain boundaries; this observation confirms that secondary phases based on  $Mg_2Al_3$  were massively formed along the  $\alpha$ -Al dendritic boundaries. As is shown in Figure 4(a) and 4(b), the GBPs are discretely precipitated at the grain boundaries in Al-2.5Mg and Al-4.5Mg. With increasing Mg content, the distribution of GBPs increases. This result indicates that the more discontinuous the distribution of GBPs, the better the resistance of the studied alloy to SCC. These results are later compared with the SCC susceptibility results obtained in electrochemical tests and with the observed SCC behavior.

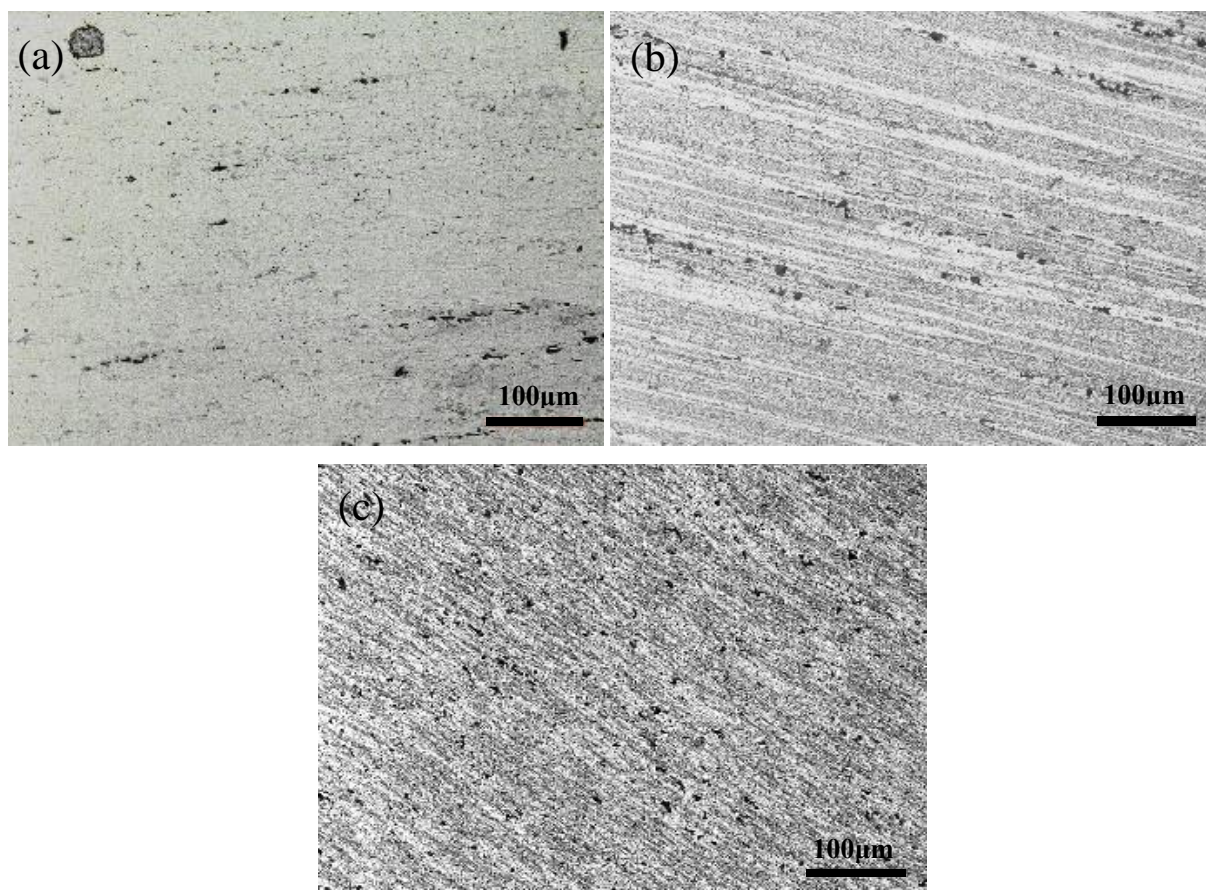


**Figure 3.** Microstructure of the as-received Al-Mg alloys (a) Al-2.5Mg (b) Al-4.5Mg (c) Al-6.3Mg

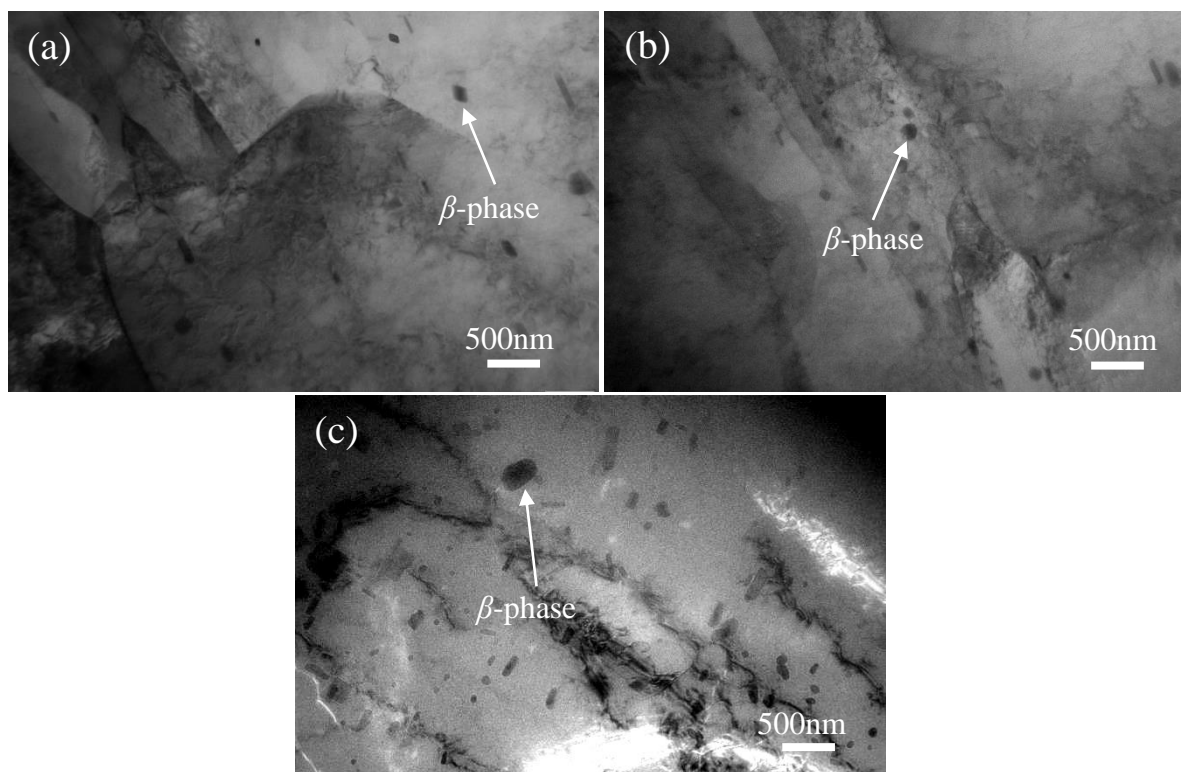


**Figure 4.** Microstructure of the as-received Al-Mg alloys (observed by TEM) (a) Al-2.5Mg, (b) Al-4.5Mg, and (c) Al-6.3Mg

### 3.2 Electrochemistry of Al-Mg Alloys

To predict the corrosion susceptibility of the Al-Mg alloys with different Mg contents, electrochemistry tests were performed on the Al-2.5Mg, Al-4.5Mg, and Al-6.3Mg alloys in 3.5 wt.% NaCl solution. The change in the OCP with the Mg content in the Al-Mg alloys is shown in Figure 5. As can be seen in Figure 5, the OCP decreases linearly with an increase in Mg content, which reveals that the Al-Mg alloys tend to become more prone to corrosion with increasing Mg content.

The sensitivity to corrosion initiation corresponds to a lower corrosion potential ( $E_{\text{corr}}$ ), and greater corrosion current density ( $i_{\text{corr}}$ ) value suggests higher corrosion rates. Figure 6 exhibits the potentiodynamic curves for Al-2.5Mg, Al-4.5Mg, and Al-6.3Mg alloys immersed in 3.5 wt.% NaCl solution for (a) 0 days and (b) 42 days. For the curves whose potential change is not obvious, the potential at which the current density reaches 100  $\mu\text{A}$  is defined as the pitting potential ( $E_{\text{pit}}$ ). As shown in Figure 6, both the  $E_{\text{corr}}$  and  $E_{\text{pit}}$  decrease with an increase in Mg content. This is because the presence of  $\beta$ -phase precipitates causes pitting at the particle-matrix interface [27]. The  $E_{\text{corr}}$  determined from the Al-6.3Mg polarization curve is approximately 721 mV, which is more negative than those determined from the polarization curves of the Al-2.5Mg and Al-4.5Mg alloys. Baldwin also found that in Al-Mg alloys in the brine environment, the corrosion current density increases with increasing Mg content [28]. This performance difference is more obvious in the polarization curves of Al-Mg alloys immersed in 3.5 wt.% NaCl solution for 42 days (Figure 6(b)), thus indicating that the corrosion susceptibility of the Al-Mg alloys increases with an increase in Mg content.

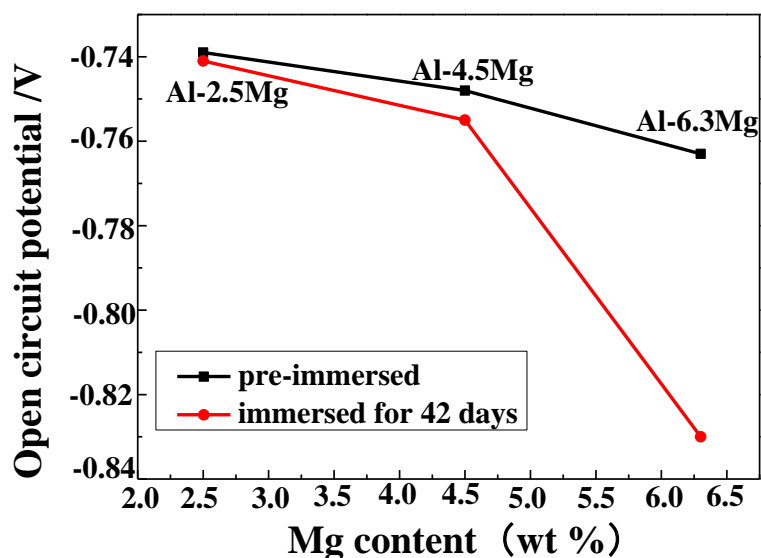


Figure 5. Open circuit potential of Al-Mg alloys

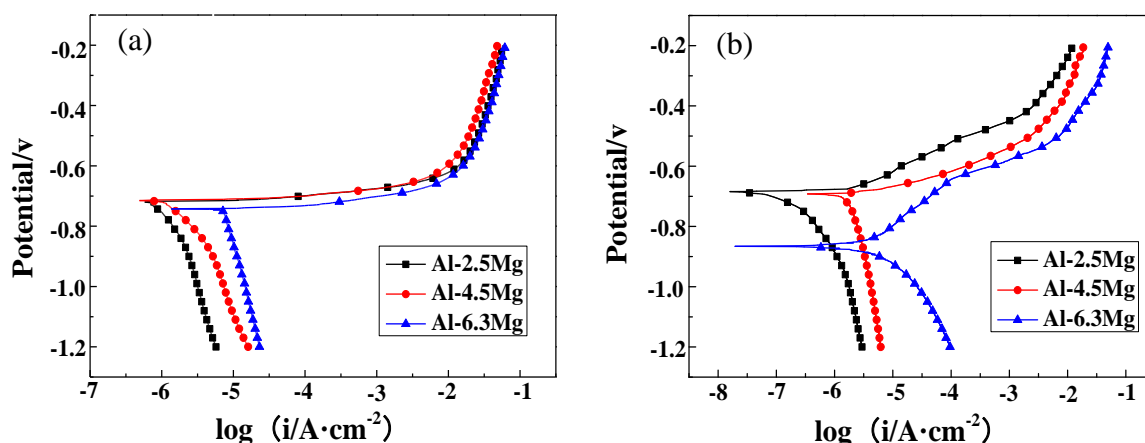


Figure 6. Polarization curves of Al-Mg alloys (a) pre-immersed, (b) immersed for 42 days

Notably, the Al-2.5Mg alloy exhibits the lowest  $i_{corr}$ , indicating that the Al-2.5Mg exhibits the lower corrosion rate among the three compositions. When the Mg content is greater than 3.5 wt.%, the corrosion rate of the Al alloys increases rapidly with an increase in Mg content, which is attributed to  $\beta$ -phase precipitation along the grain boundaries. Compared with Al matrix, the  $\beta$ -phase has lower  $E_{corr}$  and stronger anodic activity, resulting in tendency to dissolution in corrosive electrolytes [29, 30]. The activity of the  $\beta$ -phase can account for the occurrence of SCC along the grain boundaries of Al alloys. With an increase in Mg content, pitting corrosion and SCC become more severe, particularly when the alloys are immersed in a solution containing  $Cl^-$ .

EIS was performed on the three Al-Mg alloys to research the role of their Mg content in their electrode reaction processes. Figure 7 exhibits the Bode plots for the pre-immersed Al-Mg alloys, and Figure 8 shows the Bode plots for the Al-Mg alloys which were immersed in 3.5 wt.% NaCl solution for 42 days. As is exhibited in the figure, there are almost no difference at high frequencies, and the

samples electrode behaviors are dominated by double-layer capacitance. The slopes of the impedance-frequency curves in Figures 7(b) and 8(b) show that the electrodes exhibit absolute capacitance behavior. Generally, anti-corrosion capacity corresponds to the impedance peak at low frequencies [31]. Figures 7(a) and 8(a) show that the impedance of the alloy substrates ranges from  $10^3$  to  $10^5 \Omega \cdot \text{cm}^2$  at low frequencies. Figures 7(a) and 8(a) also show that the impedance of the Al-Mg alloys decreases with an increase in Mg content, implying that the anti-corrosion capacity of the Al-Mg alloys decreases with increasing Mg content. In addition, the Al-2.5Mg alloy exhibits the best corrosion performance among the three investigated alloy compositions. Furthermore, the argument curves in the Bode phase diagram in Figures 7(b) and 8(b) indicate that the phase angles increase monotonically with increasing frequency in the low frequency range but decrease monotonically at higher frequencies.

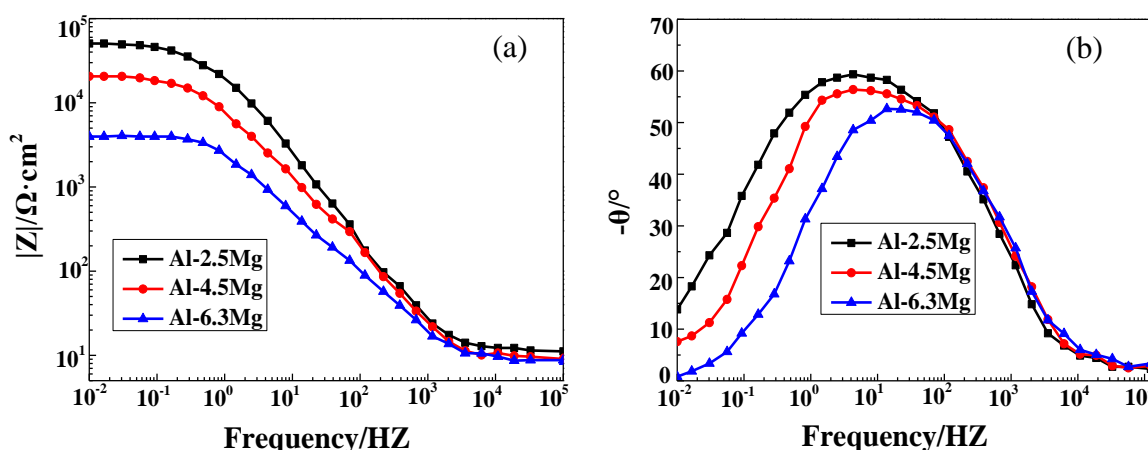


Figure 7. Bode plots of pre-immersed Al-Mg alloys (a) Bode  $|Z|$  diagram, (b) Bode phase diagram

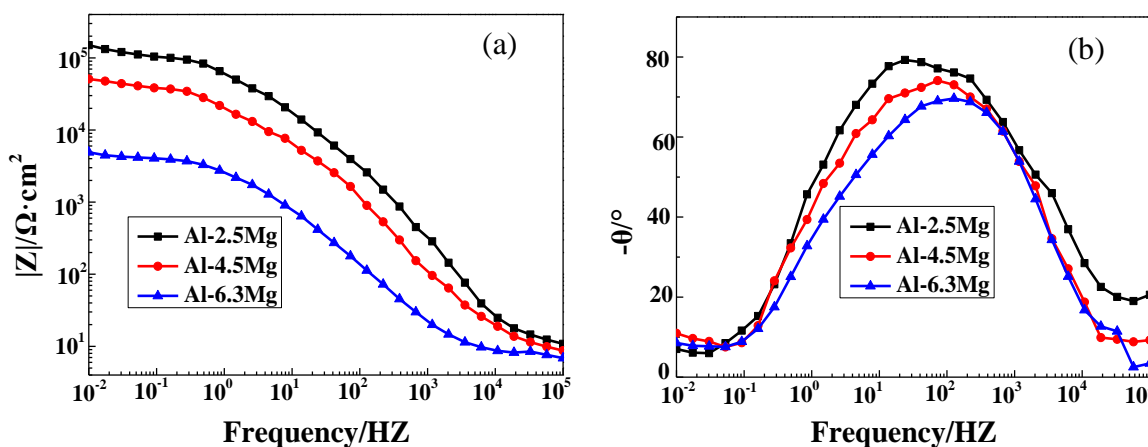
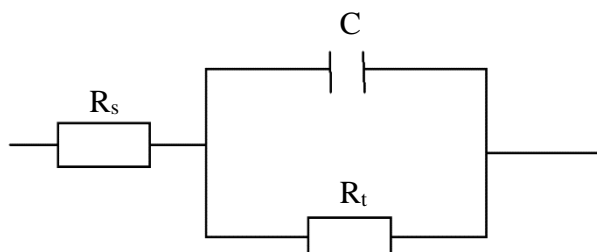


Figure 8. Bode plots of Al-Mg alloys immersed in 3.5 w.t% NaCl solution for 42 days (a) Bode  $|Z|$  diagram, (b) Bode phase diagram

EIS of the Al-Mg alloys at different immersion time are simulated using suitable equivalent circuit based on the characteristic of EIS in the corrosion process, as exhibited in Figure 9,  $R_s$

represents the solution resistance, C is the double-layer capacitance of the solution, and  $R_t$  is the charge transfer resistance. The test solutions were identical, and the insignificant differences in  $R_s$  are attributed to the hydrogenation reaction, which causes an increase in the resistance between the working electrode and the reference electrode.  $R_t$  can be substituted for the impedance value as  $R_s$  is insignificant compared with  $R_t$ , where higher  $R_t$  values indicate better anti-corrosion performance. The results of Zsimpwin software simulation are indicated in Table 2. Notably, Al-2.5Mg exhibits the highest  $R_t$  among the investigated alloys, implying that it exhibits the best anti-corrosion performance, identical to the aforementioned experimental results.



**Figure 9.** The equivalent circuit of galvanic corrosion for different composites

**Table 2.** Parameters of Equivalent Circuits for Different Composites

Materials	Pre-Immersed			Immersed for 42 days		
	Al-2.5Mg	Al-4.5Mg	Al-6.3Mg	Al-2.5Mg	Al-4.5Mg	Al-6.3Mg
$R_s(\Omega \cdot \text{cm}^{-2})$	11.62	13.21	13.97	10.642	11.836	11.163
$R_t(\Omega \cdot \text{cm}^{-2})$	55413	29080	3658	109640	47184	3934

Dutta [32] has made the point of view that, the stress corrosion of metal matrix composites is more serious than that of matrix because of the large thermal stress around the substrate during the manufacturing process. However, this stress corrosion is not the main corrosion factor. After the surface pitting penetrates the Al alloy surface, the corrosive medium penetrates into the inner layer of the material. Electrochemical corrosion is prone to more severe and sustained corrosion along the fiber matrix is rapidly expanding. Electrochemical corrosion tests mainly analyze the corrosion between the fibers and the matrix of the alloy. Because the electrode potential of a Pt electrode is substantially greater than that of an Al-Mg alloy, the Al-Mg alloy has a higher corrosion rate, which can be interpreted with the following reactions:



### 3.3 Effect of Mg Content on SCC Behavior

The SCC susceptibility and fracture mechanism of Al-Mg alloys with various Mg contents cannot be determined only from polarization curves; they should be verified through a combination of mechanical measurements. Mondolfo [33] has shown the point of view that, Mg content is the main

factor affecting the mechanical properties of commercial Al-Mg alloys. To research the effect of Mg content in Al-Mg alloys, we conducted SCC tests on the Al-2.5Mg, Al-4.5Mg, and Al-6.3Mg specimens.

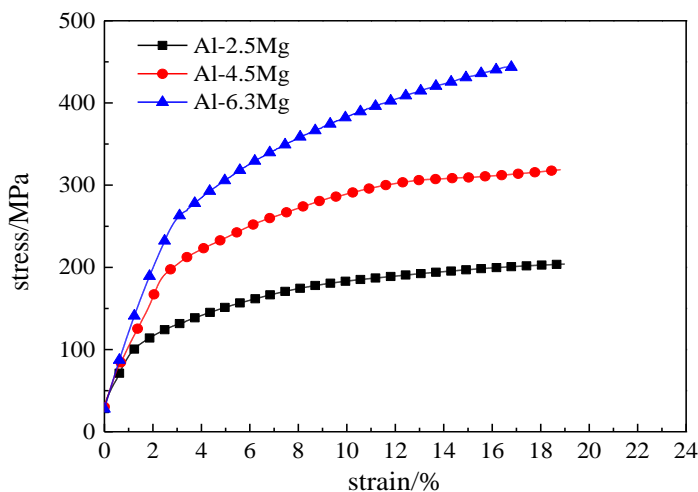


**Figure 10.** Typical constant extension rate test curves of Al-Mg alloys in 3.5 wt.% NaCl solution after immersing in 3.5 wt.% NaCl solution for 14 days

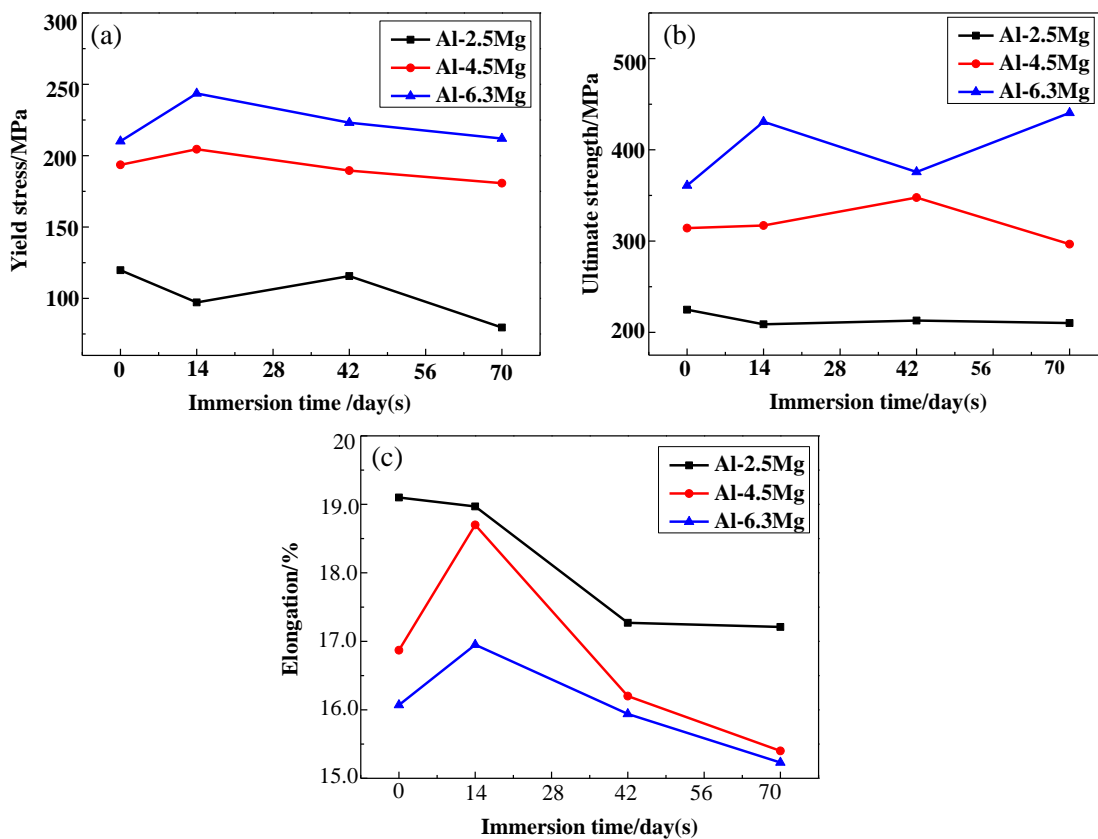


**Figure 11.** Static material properties of Al-Mg Alloys (a) Yield stress  $\sigma_y$  (MPa), (b) Ultimate strength  $\sigma_u$  (MPa), and (c) Fracture strain  $\epsilon_f$  (%)

Collinear bilateral pulls along double-sided specimens were used in the mechanical performance test. The experiments were performed on specimens according to the dimension exhibited in Figure 2. Constant extension rate tests were carried out in 3.5 wt.% NaCl solution, the specimens were pre-immersed and immersed in 3.5 wt.% NaCl solution for 14, 42, 70 days respectively, constant extension rate test curves of three alloys in 3.5 wt.% NaCl solution after immersing for 14 days are exhibited in Figure 10, average values of the material properties are shown in Figure 11.

The highest yield stress and ultimate strength are observed for the Al-6.3Mg alloy because the added Mg substantially strengthens the alloys [34]. By contrast, the Al-2.5Mg alloy exhibits the best ductility, which indicates lower SCC susceptibility.

SEM micrographs in Figure 12 has shown the stress corrosion fracture surface of Al-4.5Mg immersed in 3.5 wt.% NaCl solution for 14 days, a) in Figure 12 is the high magnification image and b) in Figure 12 is the low magnification image of fracture surface respectively. The fracture is chiefly intergranular and transgranular and the stress corrosion crack surface is mainly IGC. SCC initiation is closely related with the initiation as well as the propagation of localized corrosion, especially the IGC [35]. SEM fractographs of the Al-4.5Mg immersed in NaCl solution show substantial brittleness. These investigations are consistent with previous fractographs reported for a similar material [36]. The SCC susceptibility of a metal depends on its GBPs. In the case of the Al-Mg alloys, specimens with a high Mg content, such as Al-4.5Mg and Al-6.3Mg, exhibited intergranular SCC and greater susceptibility to SCC.

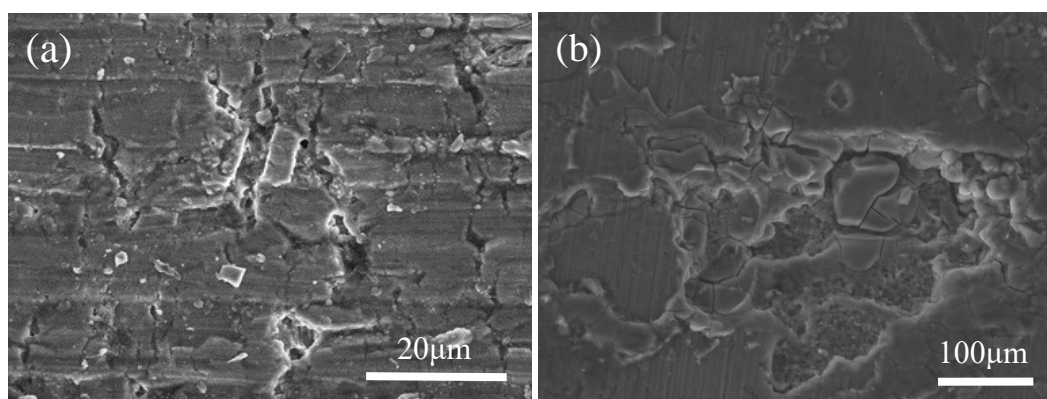


**Figure 12.** Fracture surface of Al-4.5Mg Alloy immersed 3.5 wt.% NaCl solution for 14 days(a) high magnification (b) low magnification

For notched specimens, the SCC resistance of Al-Mg alloys in corrosive electrolyte can be estimated by the crack growth rate ( $da/dt$ , m/s) and threshold stress intensity factor for SCC ( $K_{ISCC}$ ) [37]. As regards a commercially produced middle-strength Al alloy, the  $da/dt$  vs  $K_I$  curve shows two distinguishable stages roughly [38]. The  $da/dt$  increases sharply with increasing  $K_I$  in stage I, whereas it increases gently in stage II. Lee [39] has demonstrated that SCC is mainly controlled by anodic dissolution (AD) in stage I and by hydrogen embrittlement in stage II.

Collinear bilateral pulls along double-sided specimens of Al-Mg alloys were used in SCC experiments. According to the dimension of the sample exhibited in Figure 2, the stress intensity factor ( $K_I$ ) can be predicted by the following equation:

$$K_I = F\sigma\sqrt{\pi a} \tag{1}$$

where  $F$  is the geometric parameter of the specimen, which is obtained from the appropriate graph in the Stress Intensity Factor Handbook [40],  $a$  is the crack length recorded with a reading microscope, and  $\sigma$  is the stress calculated according to the external load  $P$ , which was recorded by a transducer. The  $da/dt$  was obtained from the measurement data of the crack length as a function of time by taking the derivative of the fitting curve for the middle point.

In experimental practice, the minimal value of  $K$  from the diagram of  $da/dt$  vs applied stress intensity to failure is generally called the  $K_{ISCC}$ . Which has been marked in  $da/dt$ - $K_I$  curves, as is shown in Figure 13, there is typical power function relation between  $da/dt$  and the applied load level ( $K_I$ ). Indeed, threshold-like behavior is noticed in the experiments; when the  $K_I$  approaches the  $K_{ISCC}$ , the  $da/dt$  tends to be constant ( $10^{-10}$  m/s).  $K_{ISCC}$  of Al-2.5Mg is about  $2.2 \text{ MPa}\cdot\text{m}^{1/2}$ ,  $K_{ISCC}$  of Al-4.5Mg is about  $3.5 \text{ MPa}\cdot\text{m}^{1/2}$ ,  $K_{ISCC}$  of Al-6.3Mg is about  $7.3 \text{ MPa}\cdot\text{m}^{1/2}$ . Whereas, the crack-growth behavior during stage II substantially differs from that during stage I. In stage I, when  $K_I$  is larger than  $K_{ISCC}$ , the crack propagates at low speed and the  $da/dt$  increases rapidly with the increase of  $K_I$ , the mechanical factor plays a major role; in stage II, when  $K_I$  increases to a certain value,  $da/dt$  almost remains constant, chemical factors play a major role.

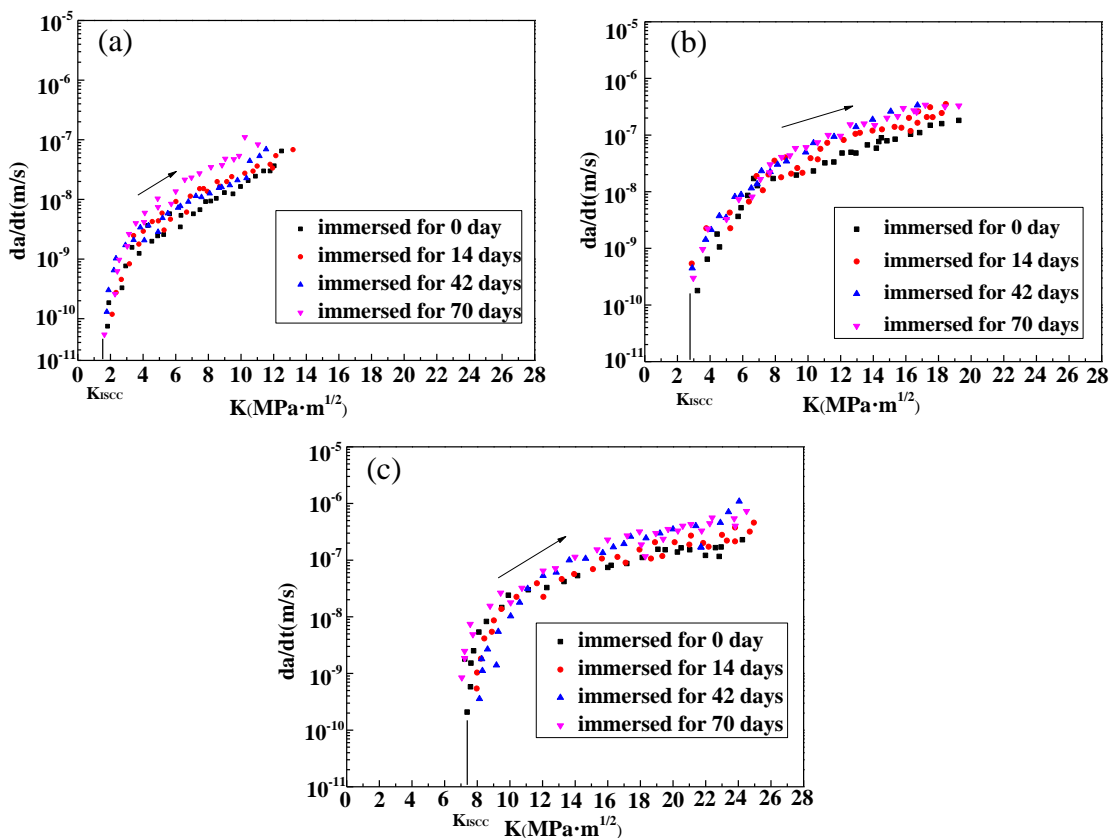


**Figure 13.** Stress corrosion crack growth rate curves of Al-Mg Alloys (a) Al-2.5Mg, (b) Al-4.5Mg, and (c) Al-6.3Mg

The crack-growth behavior during stage I of the SCC tests reveals that the initial crack-growth rate is mainly up to the stress intensity factor, then returns to a stable crack-growth rate during stage II. As exhibited in Figure 11, the Al-2.5Mg alloy shows a lowest  $K_{ISCC}$  because of its low strength performance, whereas the slopes of the  $da/dt-K_I$  curves during stage II increase with an increase in Mg content in the Al-Mg alloys and  $da/dt$  of Al-6.3Mg is the fastest at a given stress intensity factor, thus implying that stress corrosion is more and more serious with the increase of Mg content in the Al-Mg alloys.

The above results are consistent with the mechanism of AD or H-induced crack propagation. The recent reports of Windisch [41] indicate that elemental Mg can accelerate the dissolution of the  $\beta$ -phase, which can support anodic dissolution.

#### 4. CONCLUSIONS

The effects of the Mg content of Al-Mg alloys on their SCC properties were investigated using different methods. The results have led to following conclusions.

(1) The  $\beta$ -phase precipitation along the grain boundaries of Al-Mg alloys increases with increasing Mg content, resulting in the grain boundaries more likely to be affected by IGC.

(2) Both the  $E_{corr}$  and  $E_{pit}$  decrease with an increase in Mg content, indicating that the corrosion susceptibility of the Al-Mg alloys increases with an increase in Mg content. The Al-2.5Mg alloy exhibits the lowest  $i_{corr}$ , implying that it exhibits the best anti-corrosion performance, identical to the EIS results.

(3) As for the SCC tests, the highest yield stress and ultimate strength were observed in the Al-6.3Mg alloy because the added Mg substantially increased the strength of the alloys. Whereas the Al-2.5Mg alloy exhibited the best ductility, which implied lower SCC susceptibility. Furthermore, the slopes of the  $da/dt-K_I$  curves during stage II increase with an increase in Mg content in the Al-Mg alloys and  $da/dt$  of Al-6.3Mg is the fastest at a given stress intensity factor, implying that stress corrosion is more and more serious with the increase of Mg content in the Al-Mg alloys.

#### ACKNOWLEDGEMENTS

The authors gratefully acknowledge the financial support of the National Natural Science Foundation of China (51574147, 51790481) and Natural Science Foundation of Liaoning Province (201602474).

#### References

1. R. H. Jones, D. R. Baer and M. J. Danielson, *Metall.Mater.Trans.A.*, 32 (2001) 1699.
2. Y. Xu, Y. Li, J. Yang, S. Sang and Q. Wang, *Metall. Mater. Trans.B.*, 48 (2017) 1763.
3. D. S. D'Antuono, J. Gaies and W. Golumbskie, *Acta Mater.*, 123 (2017) 264.
4. N. M. Anas, W. L. Quah and H. Zuhailawati, *Procedia.Chem.*, 19 (2016) 241.
5. Z. T. Zhang, T. Matsushita, W. C. Li and S. Seetharaman, *Metall. Mater. Trans.B.*, 38 (2007) 231.

6. M. N. James, D. J. Hughes and D. G. Hattingh, *Int. J. Fatigue.*, 31 (2009) 28.
7. Z. Y. Cui, X. G. Li and K. Xiao, *J. Mater. Eng. Perform.*, 24 (2015) 296.
8. N. B. Ali, R. Estevez and D. Tanguy, *Eng. Fract. Mech.*, 97 (2013) 1.
9. N. J. H. Holroyd, T. L. Burnett and M. Seifi, *Mater. Sci. Eng. A.*, 682 (2017) 613.
10. J. Yan and A. M. Hodge, *J. Alloys Compd.*, 703 (2017) 242.
11. X. He, Z. Yan and H. Liang, *J. Mater. Eng. Perform.*, 26 (2017) 2226.
12. R. L. Holtz, P. S. Pao and R. A. Bayles, *Metall. Mater. Trans. A.*, 43 (2012) 2839.
13. G. Yi, D. A. Cullen and K. C. Littrell, *Metall. Mater. Trans. A.*, 48 (2017) 1.
14. T. L. Su, S. S. Wang and L. C. Tsao, *J. Mater. Eng. Perform.*, 11 (2002) 187.
15. J. Zhang, S. Kalnaus and M. Behrooz, *Metall. Mater. Trans. A.*, 42 (2011) 448.
16. J. Buczynski and R. Kelly, *J. Immunoassay.*, 35 (2011) 428.
17. R. G. Song, M. K. Tseng and B. J. Zhang, *Acta Mater.*, 44 (1996) 3241.
18. M. Liu, P. Schmutz and S. Zanna, *Corros. Sci.*, 52 (2010) 562.
19. M. Liu, S. Zanna and H. Ardelean, *Corros. Sci.*, 51 (2009) 1115.
20. J. B. Hao, X. D. Li and Z. T. Mu, *Mater. Des.*, 88 (2015) 331.
21. A. K. Syed, X. Zhang and J. E. Moffatt, *Int. J. Fatigue.*, 98 (2017) 53.
22. N. Nemati, M. Emamy and A. R. Emami, *Mater. Trans.*, 53 (2012) 1310.
23. R. J. Gest and A. R. Troiano, *Corrosion*, 30 (1974) 274.
24. H. P. Seifert and S. Ritter, *J. Nucl. Mater.*, 378 (2008) 312.
25. "Standard Test Method for Measurement of Fatigue Crack Growth Rates", E647 (2008) *ASTM*.
26. A. S. Kobayashi and M. Ramulu, *J. Appl. Mech.*, 59 (1985) 245.
27. N. Birbilis, M.K. Cavanaugh, R.G. Buchheit, *Corros. Sci.*, 48 (2006) 4202.
28. K.R. Baldwin, R.I. Bates, R.D. Arnell, C.J.E. Smith, *Corros. Sci.*, 38 (1996) 155.
29. S. Vuelvas, S. Valdez and J. G. Gonzalez-Rodriguez, *Int. J. Electrochem. Sci.*, 7 (2012) 4171.
30. J. Li, K. Wan, N. Wang, *Int. J. Electrochem. Sci.*, 12 (2017) 3030.
31. X. Wang, G. Chen and W. Yang, *Metall. Mater. Trans. A.*, 41 (2010) 3458.
32. I. Dutta, *J. Electrochem. Soc.*, 138 (1991) 3199.
33. L. F. Mondolfo, *Butter Worths*, 31 (1976) 651.
34. L. Vrsalovic, M. Kliskic, S. Gudic, *Int. J. Electrochem. Sci.*, 4 (2009) 1568.
35. Q.Q. Sun, K.H. Chen, H.C. Fang, J. Xu, P.X. Dong, G.Y. Hu and Q.Y. Chen, *Int. J. Electrochem. Sci.*, 11 (2016) 5855.
36. W. Y. Chu, C. M. Hsiao and J. W. Wang, *Acta Mech. Sin.*, 16 (1985) 1663.
37. R. E. Ricker, E. U. Lee and R. Taylor, *Metall. Mater. Trans. A.*, 44(2013) 1353.
38. M. O. Speidel, *Metall. Mater. Trans. A.*, 6 (1975) 631.
39. S. M. Lee, S.I. Pyun and Y. G. Chun, *Metall. Mater. Trans. A.*, 22A (1991) 2407.
40. Y. E. Murakami, *J. Appl. Mech.*, 1 (1987) 1063.
41. W. Wen, Y. Zhao and J. G. Morris, *Mater. Sci. Eng. A.*, 392 (2005) 136.